An Observational Estimate of the Pattern Effect on Climate Sensitivity: The Importance of the Eastern Tropical Pacific and Land Areas

DAVID W. J. THOMPSON,[a,c] MARIA RUGENSTEIN,[a] PIERS M. FORSTER,[b] AND LEIF FREDERICKS[a]

[a] *Department of Atmospheric Science, Colorado State University, Fort Collins, Colorado*
[b] *School of Earth and Environment, University of Leeds, Leeds, United Kingdom*
[c] *School of Environment Sciences, University of East Anglia, Norwich, United Kingdom*

(Manuscript received 14 December 2023, in final form 11 April 2025, accepted 15 April 2025)

ABSTRACT: The patterns associated with the top-of-the-atmosphere radiative response R to surface temperature T are typically explored through two relationships: 1) the spatially varying radiative response to spatially varying changes in temperature ($\Delta R_i/\Delta T_i$) and 2) the spatially varying radiative response to global-mean changes in temperature ($\Delta R_i/\Delta T$). Here, we explore the insights provided by an alternative parameter: the global-mean radiative response to changes in spatially varying temperature ($\Delta R/\Delta T_i$). The pattern $\Delta R/\Delta T_i$ indicates regions where surface temperature covaries with R and thus provides a statistical analog to the causal response functions derived from atmospheric Green's function experiments. The pattern can be transformed so that it can be globally averaged and thus indicates the local contribution to the global feedback parameter. The transformed version of $\Delta R/\Delta T_i$ corresponds to the pattern in surface temperature whose expansion coefficient time series explains the maximum fraction of the covariance between R and T_i. It explains roughly the same fraction of internal variability in R as that explained by the Green's function approach.

We focus on the physical insights provided by $\Delta R/\Delta T_i$ when it is estimated from regression analyses of monthly mean observations. Consistent with the results of Green's function experiments, the observational analyses indicate negative contributions to the global internal feedback parameter over the western Pacific and positive contributions over the southeastern tropical Pacific. Unlike the results of such experiments, the analyses indicate notable negative contributions to the global feedback parameter over land areas. When estimated from observations, temperature variability over the land areas accounts for ~70% of the negative global internal feedback, whereas variability over the southeastern tropical Pacific reduces the global-mean negative internal feedback by ~10%.

KEYWORDS: Atmosphere; Climate; Climate sensitivity; Internal variability

1. Introduction

The response of the climate system to radiative forcing can be modeled as linearly proportional to the change in surface temperature, such that

$$N = F + R \approx F + \Lambda T, \qquad (1)$$

where F is the global-mean radiative forcing, $R \approx \Lambda T$ is the global-mean radiative response, N is the global-mean top-of-the-atmosphere (TOA) radiative imbalance, T is the global-mean surface temperature anomaly, and Λ is the linearized global climate feedback parameter, where stabilizing feedbacks are taken to be negative (e.g., Hansen et al. 1997). If the variables in Eq. (1) are a function of time, then the global feedback parameter can be expressed as $\Lambda \approx [\Delta(N - F)/\Delta T]$, where Δ denotes the differences in a parameter with time. In the case where the global-mean radiative forcing F is constant, the global feedback parameter can be estimated as $\Lambda \approx (\Delta N/\Delta T) = (\Delta R/\Delta T)$ (e.g., see Sherwood et al. 2020 and references therein).

The radiative damping term ΛT depends not only on the global-mean surface temperature change but on the spatial pattern of the temperature change as well. There are several reasons for this. One, the amplitude of local feedback processes depends on the local temperature change (Armour et al. 2013). If temperature does not change at a given location, then the local feedbacks operating at that location will not be "activated" and thus will not contribute to Λ. Two, the amplitude of local feedback processes may vary nonlinearly with local conditions. For example, snow and sea ice feedbacks depend on the existing snow and sea ice coverage (Boer and Yu 2003). Three, the amplitude of local feedback processes depends on remote temperature changes (e.g., Andrews et al. 2015; Gregory and Andrews 2016; Zhou et al. 2016, 2021; Dong et al. 2019, 2021; Andrews and Webb 2018; Andrews et al. 2022). For example, relatively large warming over the western tropical Pacific is associated with rising motion locally and subsidence elsewhere. If the subsidence occurs over a region of marine stratus and stratocumulus clouds such as the eastern tropical Pacific, then the low cloud feedbacks operating over such regions may be activated by warming far removed from the stratus decks (Dong et al. 2019; Andrews and Webb 2018; Andrews et al. 2022; Myers et al. 2023). The dependence of the radiative damping term on the spatial pattern of temperature change is referred to as the "pattern effect" on radiative feedbacks (e.g., Stevens et al. 2016; Gregory and Andrews 2016).

The pattern effect is important since it leads to time variability in climate sensitivity. Notably, the large warming over the western tropical Pacific juxtaposed against weak warming/

Corresponding author: David W. J. Thompson, davet@atmos.colostate.edu

DOI: 10.1175/JCLI-D-23-0737.1

cooling over the eastern tropical Pacific over the past few decades is thought to have led to a suppression of positive low cloud feedbacks over the eastern tropical Pacific and thus a larger negative global feedback parameter (e.g., Andrews et al. 2015; Gregory and Andrews 2016; Zhou et al. 2016, 2017; Dong et al. 2019; Andrews and Webb 2018; Andrews et al. 2022; Myers et al. 2023). It follows that the global feedback parameter is expected to become less negative—and thus, the climate sensitivity is expected to increase—when the eastern tropical Pacific warms (e.g., Alessi and Rugenstein 2023).

The pattern effect has been investigated extensively in numerical simulations using two primary approaches. In one approach, the global feedback parameter is calculated in numerical simulations forced with different patterns of temperature change. The difference in the global feedback parameter between a simulation forced with, say, recent observed changes in SSTs and a simulation forced with abrupt 4x carbon dioxide (CO_2) forcing provides insight into the role of recent SST trends on climate sensitivity (e.g., Andrews et al. 2015, 2022; Andrews and Webb 2018). In a second approach, the contribution of regional temperature changes to the global feedback is assessed by 1) forcing a numerical model with surface temperature patches restricted to specific regions of the World Ocean and then 2) determining the resulting changes in the TOA radiative flux (e.g., Zhou et al. 2016, 2017; Dong et al. 2019; Bloch-Johnson et al. 2024). The latter so-called Green's function approach was used in Branstator (1985) and Barsugli and Sardeshmukh (2002) in their analyses of the atmospheric response to tropical SST variability. It has been adopted in recent years to assess the impact of regional temperature changes on radiative feedbacks (e.g., Zhou et al. 2017; Dong et al. 2019; Bloch-Johnson et al. 2024; Zhang et al. 2023).

The relationships between the spatially varying temperature field and radiative fluxes have received relatively little attention in observations. Ceppi and Gregory (2017) probed the observed relationships between the spatially varying radiative fluxes and the global-mean static stability. Zhou et al. (2017) compared the output from their Green's function experiments to the regression of observed global-mean cloud radiative effects onto local temperature. Myers et al. (2023) explored the observed relationships between spatially varying cloud radiative effects and various cloud-controlling factors. We are unaware of an observational study that has explicitly quantified the linkages between the spatially varying temperature field and the global-mean radiative feedback.

The primary goals of the current study are to 1) introduce a regression-based parameter for exploring the relationships between the spatially varying temperature field T_i and the global-mean radiative response R, 2) compare the radiative response indicated by the regression-based parameter with that provided by Green's function experiments, and 3) explore the physical insights provided by the regression-based parameter when it is applied to observations and numerical output. Two notable results include the following: 1) When applied to observations, the regression-based parameter indicates large positive contributions to the global internal feedback parameter over the eastern tropical Pacific and negative contributions over land areas, and 2) when applied to the output from a control simulation run on a coupled atmosphere/ocean climate model, a transformed version of the parameter explains roughly the same fraction of internal variability in R as that explained by the output from a Green's function experiment run on the same model. Section 2 outlines the simple regression-based parameter; section 3 probes the physical insights provided by estimating the parameter in 25 years of Clouds and the Earth's Radiant Energy System (CERES) and ERA5 observations; section 4 derives a transformed version of the parameter that indicates the local contributions to the global-mean internal climate feedback; section 5 provides an interpretation of the regression-based parameter in the context of maximum covariance analysis and partial least squares regression, compares the radiative response predicted by the parameter with that derived from Green's function experiments and principal component analysis, and assesses the reproducibility of the parameter in coupled-climate models; section 6 provides a discussion and summary of the results.

2. Definitions of local climate feedbacks

The spatially varying relationships between surface temperature and the TOA radiative fluxes are commonly assessed using two different parameters (e.g., see discussions in Feldl and Roe 2013; Bloch-Johnson et al. 2020; and Hedemann et al. 2022):

1) The rate of change in the spatially varying TOA radiative response R_i relative to the rate of change in the spatially varying surface temperature T_i:

$$\lambda_i^L = \frac{\Delta R_i}{\Delta T_i}, \tag{2}$$

where the subscript i denotes a spatially varying field, $R_i \equiv N_i - F_i$, and the superscript L denotes that the relationship is based on local fluxes and local temperature;

2) The rate of change in the spatially varying TOA radiative response R_i relative to the rate of change in global-mean temperature T:

$$\lambda_i^T = \frac{\Delta R_i}{\Delta T}, \tag{3}$$

where the superscript T denotes that the relationship is based on global-mean temperature. Results based on λ_i^L may be viewed as reflecting local feedbacks (e.g., Armour et al. 2013); results based on λ_i^T may be viewed as reflecting local contributions to the global feedback parameter (Andrews et al. 2015).

Both λ_i^L and λ_i^T are widely used to explore the spatially varying covariability between surface temperature and radiative fluxes in climate models: The parameter λ_i^L yields information about the covariability between the radiative fluxes and surface temperature at a specific location, whereas the parameter λ_i^T yields information about the covariability between the radiative fluxes at a specific location and the global-mean surface temperature. Neither method provides information about the linkages between the spatial patterns of temperature variability and the global feedback parameter: The local feedbacks indicated by λ_i^L do not translate to variations in the global-mean radiative flux since, at any given location, atmospheric heat transport can influence R_i and T_i in different ways. The relationships indicated by λ_i^T are based on global-mean rather than local temperature and thus by construction do not reveal information about the spatial structure of the temperature variability.

To explore the spatial patterns of temperature variability associated with variations in the global-mean radiative flux, we explore here the rate of change in the global TOA radiative response R relative to the rate of change in local temperature T_i, that is, we define

$$\lambda_i^R = \frac{\Delta R}{\Delta T_i}, \tag{4}$$

where $R \equiv N - F$ and the superscript R denotes that the regression is based on the global-mean TOA radiative imbalance. As is the case for λ_i^T, the relationships indicated by λ_i^R may be viewed as local contributions to the global feedback parameter, but unlike λ_i^L and λ_i^T, the parameter λ_i^R by construction reveals covariability between local surface temperature changes and the global-mean radiative imbalance.

3. Application to observations

Here, we compare the insights provided by the two widely used measures of regional feedbacks λ_i^L and λ_i^T with those provided by λ_i^R in monthly mean observations. Radiative fluxes are provided by the CERES Energy Balanced and Filled Top-of-Atmosphere Edition 4.2.1 (Loeb et al. 2018, 2022); 2-m near-surface temperatures are obtained from ERA5 (Hersbach et al. 2020). Results are based on roughly 25 years of monthly data over the period March 2000–December 2024. The CERES Edition 4.2 data combine retrievals from *Terra* (March 2000–June 2002), *Terra* and *Aqua* (July 2002–March 2022), and *NOAA-20* (April 2022–December 2024). The ERA5 2-m temperature data are not strictly speaking observations but bear close resemblance to the in situ and remotely sensed temperature used in the ERA5 assimilation scheme (Hersbach et al. 2020). The patterns derived from the coarser HadCRUT5 surface temperature data (Morice et al. 2021) are qualitatively indistinguishable from those based on ERA5. Results based on numerical output are explored in section 5.

In the case of observed internal feedbacks, the parameters λ_i^L, λ_i^T, and λ_i^R can be estimated from linear regression as follows (e.g., Gregory et al. 2004):

$$\begin{aligned}\lambda_i^L &= \frac{\overline{R_i T_i}}{\overline{T_i^2}}\\ \lambda_i^T &= \frac{\overline{R_i T}}{\overline{T^2}}\\ \lambda_i^R &= \frac{\overline{R T_i}}{\overline{T_i^2}},\end{aligned} \tag{5}$$

where all variables are departures from their seasonally varying climatological mean values and the overbars denote the time mean. The terms on the rhs in Eq. (5) correspond to the linear least squares best fits between the corresponding predictor temperature time series and predictand radiative response time series. For example, the linear least squares best fit of R to T_i is given as the covariance between R and T_i divided by the variance of T_i. The key assumption when using linear regression to estimate λ is that all variations in the independent variable—in this case temperature—influence the dependent variable. In practice, variations in the temperature field include measurement error and internal variability that is not directly related to variations in the radiative flux. As such, the regressions in Eq. (5) are biased toward zero and thus underestimate the actual values; i.e., they are susceptible to regression dilution bias (e.g., Frost and Thompson 2000). Regression dilution bias influences the amplitudes of internal feedback parameters calculated using regression analysis (e.g., Proistosescu et al. 2018; Dessler and Forster 2018; Gregory et al. 2020). It does not influence the sign of the regression and thus does not change the sign of the patterns indicated here. It also does not influence the covariance which—as discussed in sections 4 and 5—is important for characterizing the spatially varying contribution of the temperature field to the global radiative response.

We estimate λ_i^L, λ_i^T, and λ_i^R by applying Eq. (5) to the CERES TOA radiative flux and surface temperature data. In all cases, we remove the long-term mean seasonal cycle and linear trends from the data as a function of location before computing the regression coefficients. Note that we assume detrending N removes the forced signal from the data to form R (e.g., Dessler and Forster 2018). As noted below, we also reproduced key results by forming R as $N - F$, where F is the radiative forcing estimate provided by the IPCC AR6. Since the results are based on monthly mean, detrended anomalies, they should be viewed as reflecting the feedbacks between temperature and radiation that arise from internal variability, rather than the feedbacks that arise in response to climate change (e.g., Dessler and Forster 2018; Lutsko and Takahashi 2018; Sherwood et al. 2020; Rugenstein and Armour 2021). All radiative fluxes are positive downward so that positive correlations indicate regions where anomalously warm conditions are associated with anomalously downward radiative fluxes (and thus suggest positive feedbacks between temperature and the radiation fields), and vice versa.

Figure 1 shows the relationships between the TOA radiative flux and surface temperature revealed by λ_i^L (left column) and λ_i^T (right column). The top panels show results for the net TOA radiative fluxes; the middle and bottom panels show results for the shortwave and longwave components of the fluxes, respectively. The relationships between R_i and T_i indicated by λ_i^L are predominantly positive across much of the globe (Fig. 1a): Months with anomalously downward local radiative fluxes are generally associated with anomalously warm local conditions, and vice versa. The most pronounced positive regression coefficients are found in the western Pacific warm pool and in regions of marine stratus and stratocumulus clouds off the western coasts of North America, South America, Spain, and southern Africa. The relationships indicated in Fig. 1a do not necessarily indicate regions that are important for the global feedback since 1) at a given location, the atmospheric heat transport can influence R_i and T_i in different ways, and 2) the two-way coupling

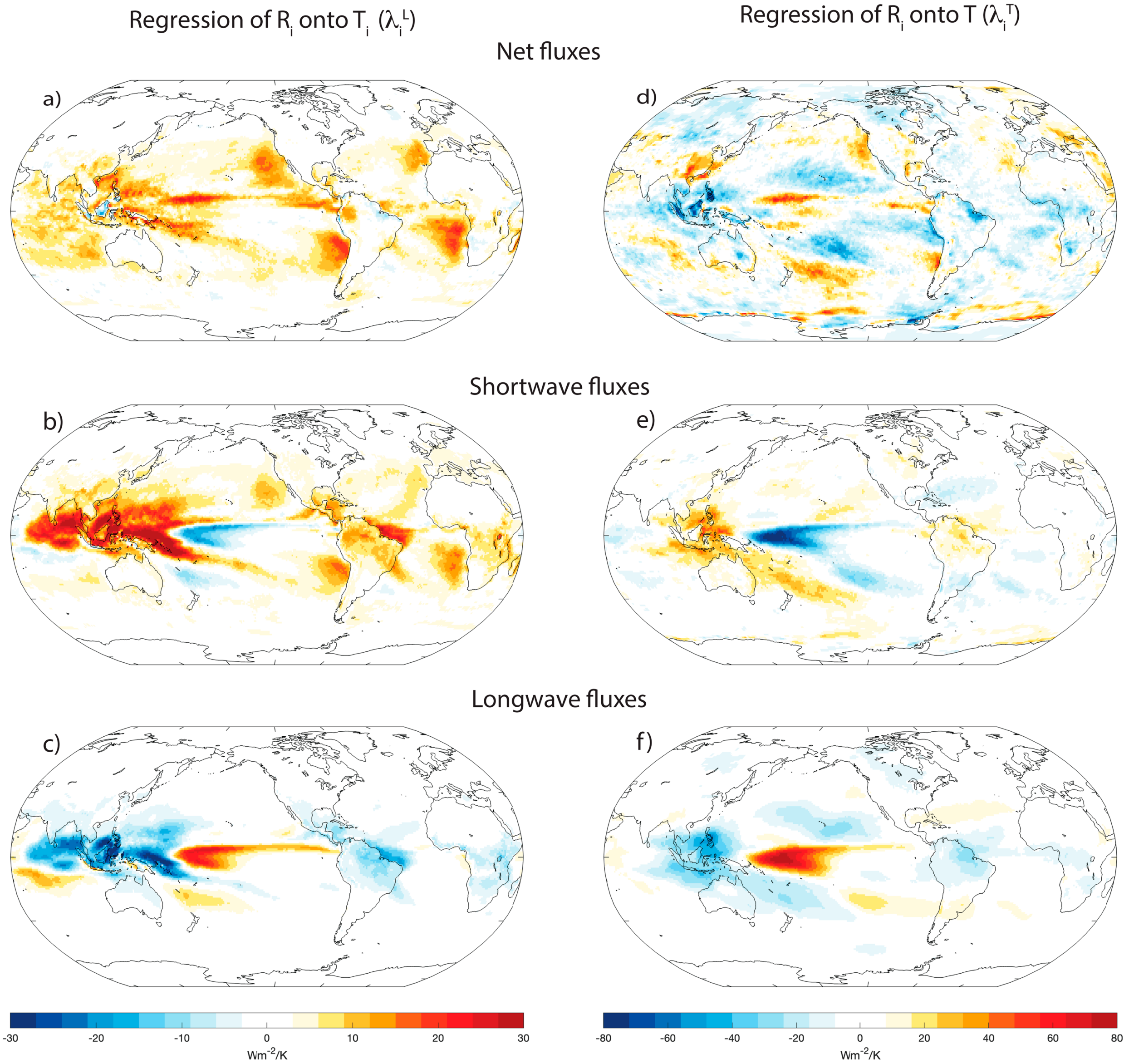

FIG. 1. (left) Regression of local TOA radiative fluxes R_i onto local surface temperature anomalies T_i for (a) net fluxes, (b) the shortwave component of the fluxes, and (c) the longwave component of the fluxes. (right) As in (left), but for the regression of local TOA radiative fluxes R_i onto global-mean surface temperature T. Results are based on monthly mean, detrended values of CERES radiative fluxes and ERA5 2-m temperature.

between radiation and temperature is pronounced at local scales, which violates the assumption in least squares regression that the dependent variable R_i responds to the independent variable T_i, but not the other way around (see also Proistosescu et al. 2018; Bloch-Johnson et al. 2020; Hedemann et al. 2022).

The positive regression coefficients between R_i and T_i indicated by λ_i^L arise primarily from variations in the shortwave components of the fluxes (Fig. 1b). The positive shortwave regression coefficients are partially offset by negative longwave regression coefficients over most of the globe, especially over regions of deep convection in the tropics. The most notable exceptions are found in areas of marine stratus and stratocumulus clouds over the western coasts of the Americas and Africa (cf. Figs. 1b,c). Both the shortwave and longwave regression coefficients are dominated by changes in cloud radiative effects (not shown). The east–west dipole in the shortwave and longwave regression coefficients in the western tropical Pacific reflects an eastward shift in the region of deep convection and their associated shortwave and longwave cloud radiative feedbacks during months when the tropical Pacific is anomalously warm (as is the case during the warm phase of the ENSO phenomenon).

Results based on λ_i^T (right column) provide a very different impression of the relationships between the TOA radiative imbalance and surface temperature. For the most part, the regression coefficients are negative over much of the globe, consistent with the dominance of the Planck feedback (Fig. 1d). Notably, the positive relationships between the radiative fluxes and surface temperature indicated by λ_i^L off the western coasts of the Americas and Africa are not apparent in λ_i^T. The shortwave and longwave components of the regression coefficients (Figs. 1e,f) are consistent with the changes in clouds associated with the ENSO phenomenon and arise at least in part since ENSO is correlated with global-mean temperature T and thus influences the covariance in Eq. (5).

Taken together, the results in Fig. 1 provide information about the covariability between local radiative fluxes and local temperature (left) and between local radiative fluxes and global-mean temperature (right), but neither methodology provides information about the relationships between the global-mean radiative flux and local temperatures. Thus, neither methodology highlights regions where local surface temperature variability is strongly related to variations in global-mean radiative flux.

Figure 2 shows results based on λ_i^R, i.e., the regression of R onto T_i [Eq. (5)]. As is the case for results based on λ_i^T, the regression coefficients given by λ_i^R are negative across most of the globe, consistent with the Planck feedback. In contrast to results based on λ_i^T, the results based on λ_i^R lend themselves to straightforward physical interpretation. The largest negative regression coefficients arise in regions of deep convection in the western tropical Pacific, the South Pacific convergence zone, the ITCZ, and the central Indian Ocean (Fig. 2a). The largest positive regression coefficients are found in the vicinity of the large marine stratocumulus deck to the west of Peru and Chile.

As discussed later in section 5, the regression coefficients indicated by λ_i^R may be viewed as a statistical analog to the output of simulations run using the Green's function approach (e.g., Bloch-Johnson et al. 2024). That is, they indicate regions where local surface temperature variability covaries with the global-mean radiative response. However, there is a key difference between the interpretation of results derived from λ_i^R and the Green's function approach: The results derived from λ_i^R arise not only from the relationships between R and local temperature but also from the relationships between R and temperatures at locations that covary with local temperature. For example, the negative values of λ_i^R over the western tropical Pacific may arise from local negative feedbacks or from negative feedbacks occurring over locations where the temperature field covaries with that in the western tropical Pacific. In contrast, the changes in R indicated by the Green's function approach arise entirely from the prescribed changes in SSTs (or the attendant free-running changes in land surface temperature). The relationships between results based on regression analysis and the output from Green's function experiments are discussed in more detail in section 5.

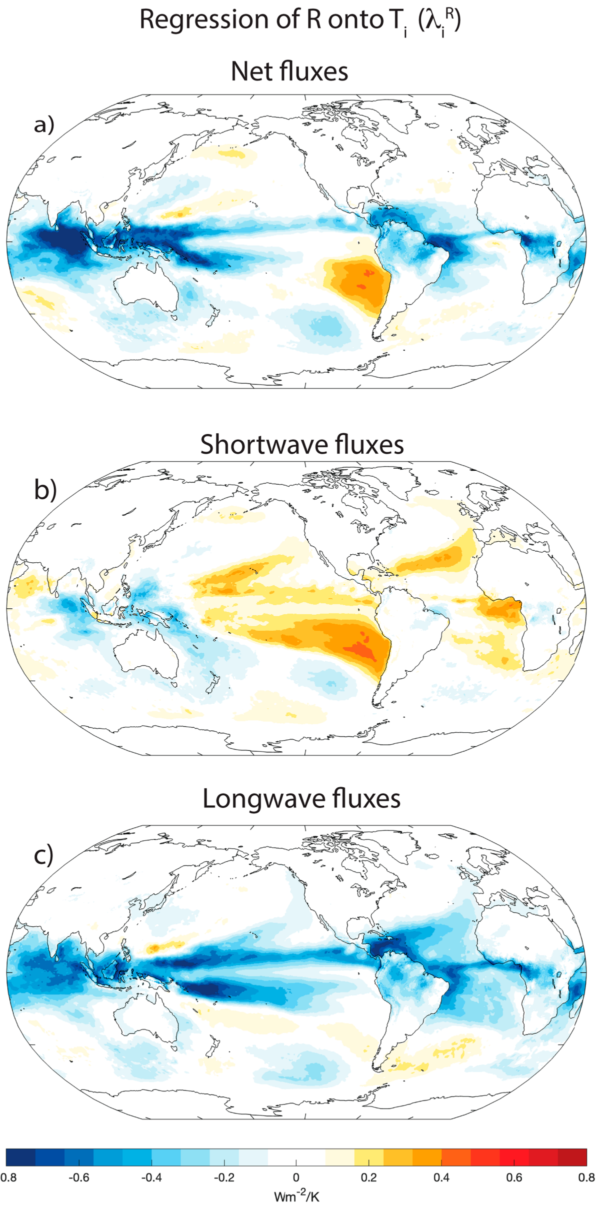

FIG. 2. Regression of global-mean TOA radiative fluxes R onto local surface temperature anomalies T_i for (a) net fluxes, (b) the shortwave component of the fluxes, and (c) the longwave component of the fluxes. Results are based on monthly mean, detrended values of CERES radiative fluxes and ERA5 2-m temperature.

Despite the differences between the regression-based and Green's function approaches, the primary features in Fig. 2a are clearly consistent with our understanding of spatially varying climate feedbacks. The negative regression coefficients over the Maritime Continent are robust in all existing Green's function-type experiments and are consistent with negative feedbacks between surface temperature anomalies and the global radiative response in regions of atmospheric deep convection (e.g., Fig. 5a in Dong et al. 2019; Fig. 2 in Bloch-Johnson et al. 2024). The positive coefficients to the west of South America are similarly found in most Green's function-type experiments and are consistent with positive local feedbacks associated with marine stratus and stratocumulus clouds (Klein and Hartmann 1993; Wood and Bretherton 2006; Andrews et al. 2015; Zhou et al. 2016; Ceppi and Gregory 2017; Andrews and Webb 2018; Dong et al. 2019; Myers et al. 2021). The absence

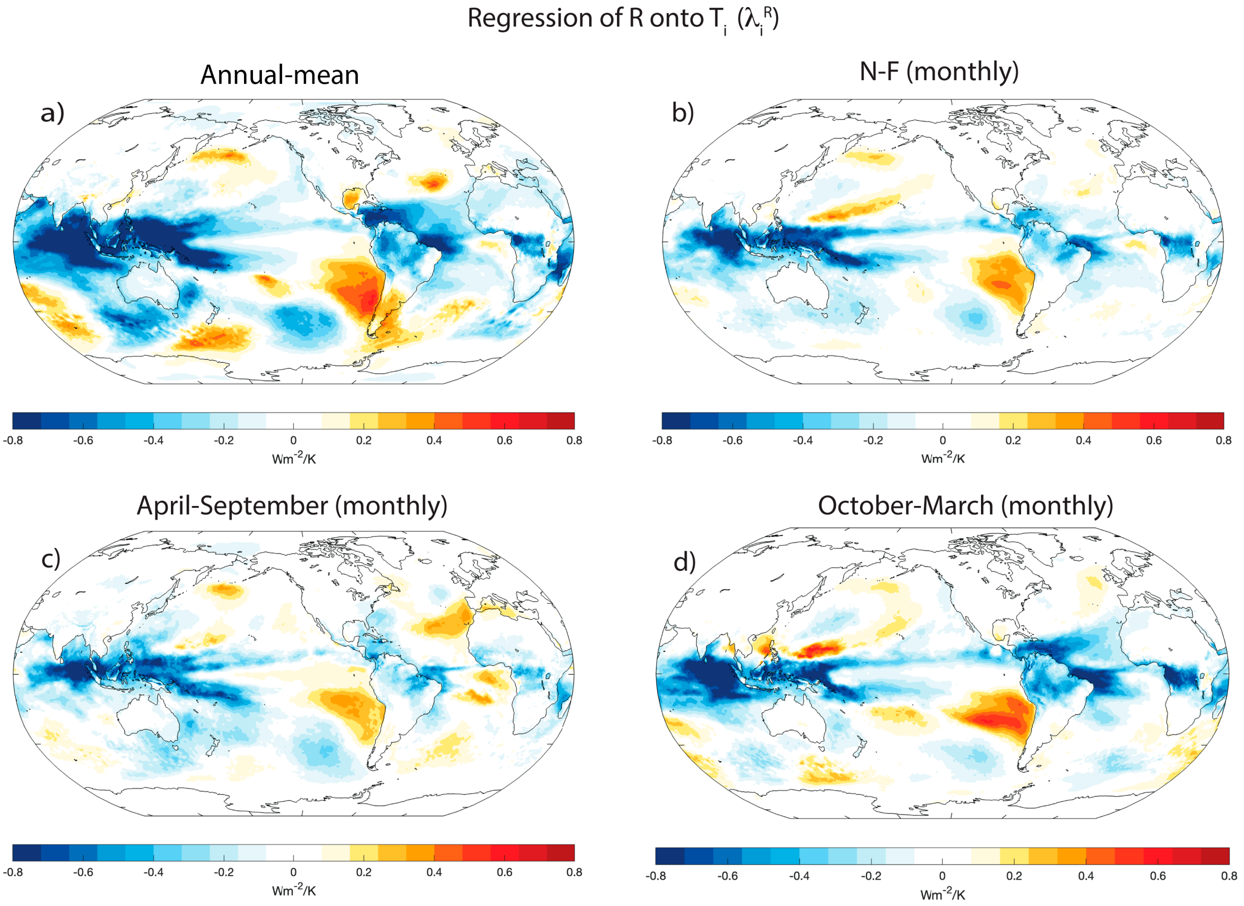

FIG. 3. As in Fig. 2a, but for (a) detrended annual-mean data, (b) monthly mean data where the forced signal in the global-mean radiative flux is removed by subtracting the radiative forcing estimate provided in chapter 7 of the IPCC Sixth Assessment Report, (c) detrended monthly mean data for April–September, and (d) detrended monthly mean data for October–March.

of positive regression coefficients over other regions of marine stratus and stratocumulus clouds—such as the west coast of North America—is notable. It suggests that the positive feedbacks between SSTs and the radiative fluxes in such regions are offset by the covariability between the temperature field and negative feedbacks arising elsewhere.

The primary features in Fig. 2a—namely, the negative values over the western tropical Pacific and positive values over the eastern tropical Pacific—are not sensitive to details of the analysis procedure. They are reproducible in analyses based on annual-mean (rather than monthly mean) versions of the data (Fig. 3a); when the analyses are repeated for subsets of the data corresponding to the months of April–September (Fig. 3c) and October–March (Fig. 3d); and in the relationships between global-mean CERES cloudy-sky fluxes and local SSTs based on a much shorter data record (Zhou et al. 2017). They are reproducible when the forced signal in the global-mean radiative flux is removed not by detrending *R* (as done in Fig. 2a) but by subtracting the radiative forcing estimate provided in chapter 7 of the IPCC Sixth Assessment Report (Forster et al. 2021) (Fig. 3b). They are statistically significant. As shown in Fig. A1 in the appendix, the *t* scores associated with the regression coefficients in Fig. 2a exceed the 95% significance level over the western tropical Pacific, tropical South America, and the equatorial regions of Africa. They exceed the 99% significance level (*t* scores exceed 4) over the southeastern tropical Pacific (see the appendix for details).

The shortwave components of λ_i^R are generally positive (Fig. 2b), consistent with higher-than-normal surface temperatures during periods of increased globally averaged shortwave absorption. In contrast, the longwave components of λ_i^R are generally negative (Fig. 2c), consistent with increased globally averaged emission to space when temperatures are higher than normal. The region of net positive coefficients to the west of South America derives from positive shortwave coefficients that are not offset by negative longwave coefficients. As is the case for results based on λ_i^L and λ_i^T, the east–west dipole in shortwave radiative feedbacks in the central Pacific is consistent with the signature of ENSO in tropical clouds (e.g., Park and Leovy 2004) and tropical radiative fluxes (e.g., Ceppi and Fueglistaler 2021).

Overall, the primary oceanic features in λ_i^R bear strong resemblance to those derived from Green's function-type experiments, notably the positive contributions to the global internal feedback parameter over the eastern tropical Pacific and the negative contributions over the western tropical Pacific. In the next section, we quantify the spatially varying contributions of the temperature field to the global internal feedback parameter, and provide evidence that land surface temperatures also play an overlooked but seemingly important role in driving the global internal climate feedback.

4. Contributions to the global-mean internal feedback parameter

The global internal feedback parameter can be estimated by regressing detrended, monthly mean values of R onto T (e.g., Dessler and Forster 2018). It is $\Lambda \approx -1.1\ \mathrm{W\,m^{-2}\,K^{-1}}$ when estimated from 25 years of CERES and global-mean 2-m temperatures from ERA5. In the case of the widely used spatially varying parameter λ_i^T, the global internal feedback parameter can be recovered by simply taking the global average of λ_i^T (e.g., Andrews et al. 2015; Hedemann et al. 2022). That is,

$$\Lambda = \langle \lambda_i^T \rangle = \left\langle \frac{\overline{R_i T}}{\overline{T^2}} \right\rangle = \frac{\overline{RT}}{\overline{T^2}},$$

where the brackets denote the global average.

In the case of the spatially varying parameter λ_i^R introduced here, the global internal feedback parameter cannot be directly recovered from λ_i^R since the denominator in the regression is a function of location [Eq. (5)]. The global feedback parameter can be recovered from the regression coefficients λ_i^R if they are first weighted by the ratio of the local to global-mean temperature variance $\overline{T_i^2}/\overline{T^2}$, that is,

$$\left\langle \lambda_i^R \frac{\overline{T_i^2}}{\overline{T^2}} \right\rangle = \left\langle \frac{\overline{RT_i}}{\overline{T_i^2}} \times \frac{\overline{T_i^2}}{\overline{T^2}} \right\rangle = \left\langle \frac{\overline{RT_i}}{\overline{T^2}} \right\rangle = \frac{\overline{RT}}{\overline{T^2}} = \Lambda,$$

where again the brackets denote the global average. We thus define a weighted local feedback parameter

$$L_i \equiv \lambda_i^R \frac{\overline{T_i^2}}{\overline{T^2}} = \frac{\overline{RT_i}}{\overline{T^2}}, \qquad (6)$$

that provides a form of λ_i^R that can be globally averaged to recover the global-mean feedback. Physically, the parameter L_i provides a quantitative estimate of the contribution of surface temperature variability over any given region to the global-mean internal feedback parameter. Statistically, the parameter may be thought of in two ways: 1) as the parameter λ_i^R weighted by the ratio of the local to global-mean temperature variances or 2) as the covariance between R and T_i normalized by the variance of T. Note the close analogy between λ_i^T and L_i: The former has $\overline{R_i T}$ in the numerator; the latter has $\overline{RT_i}$ in the numerator; and both have $\overline{T^2}$ in the denominator.

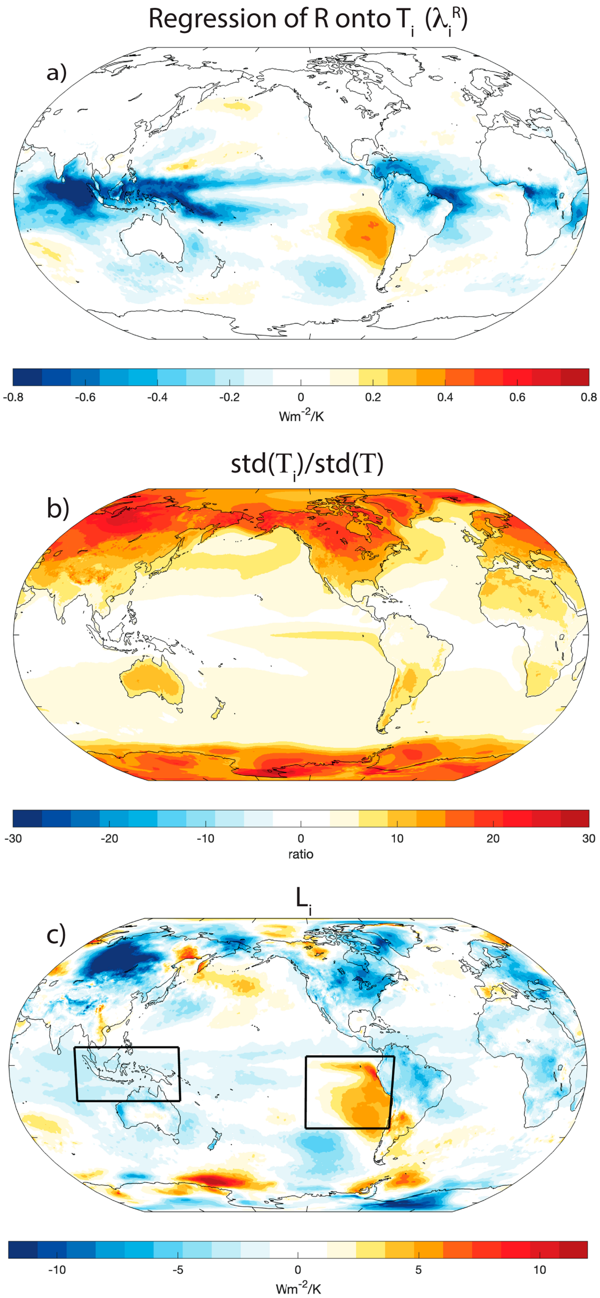

FIG. 4. (a) The local parameter λ_i^R reproduced from Fig. 2a. (b) The standard deviations of local temperature relative to global-mean temperature. (c) The form of the local parameter λ_i^R (L_i) that can be globally averaged to recover the global-mean feedback parameter. Results are based on detrended values of monthly mean CERES radiative fluxes and ERA5 2-m temperature. The boxes indicate identically sized regions used in Table 2: 90°–155°E and 10°N–20°S in the western tropical Pacific and 125°–70°W and 5°N–35°S in the eastern tropical Pacific.

Figure 4a shows λ_i^R (reproduced from Fig. 2a), Fig. 4b shows $\sqrt{\overline{T_i^2}/\overline{T^2}}$ (i.e., the square root of the weighting applied to λ_i^R), and Fig. 4c shows the weighted parameter L_i. In general, weighting λ_i^R by the local temperature variance acts to increase the amplitude of the relationships between R and T_i at high latitudes, especially over the continental areas (cf. Figs. 4a,c). That is because the regression coefficient λ_i^R is inversely proportional to the amplitude of the predictor time series T_i, whereas the covariance L_i is directly proportional to the amplitude of T_i. The inference is that the contribution of local temperatures to the global-mean radiative response depends on the amplitude of the local temperature anomaly which—in

TABLE 1. Contribution of temperature over indicated regions to the global-mean internal feedback, where the local contribution is found as $L_i \equiv (\overline{RT_i}/\overline{T^2})$ and T_i corresponds to the temperature averaged over the region indicated in the first column. Second column indicates the local contribution to Λ; third column indicates the contribution multiplied by the corresponding area of the globe; fourth column indicates the corresponding correlations and t-scores, where bold indicates t-scores significant at the two-tailed 95% level. All analyses are based on detrended, monthly mean data. Degrees of freedom are assessed taking into account the autocorrelation of the respective time series.

Region	Local contribution to Λ (W m^{-2})	Contribution (weighted by % of globe) (W m^{-2})	$r(R, Ti)$ (t score)
Globe	−1.1	−1.1	**r = −0.25 (3.6)**
Global ocean	−0.5	−0.3	r = −0.14 (1.9)
Global land	−2.4	−0.8	**r = −0.28 (4.3)**
Eastern tropical Pacific	+2.1	+0.1	**r = +0.19 (2.5)**
Western tropical Pacific	−2.1	−0.1	**r = −0.33 (4.8)**

the case of internal variability—is proportional to the local temperature variance. The large covariances over the continents indicate the prominent contribution of internal variability over land regions to monthly variations in R. The most prominent positive regression coefficients in both the unweighted (Fig. 4a) and weighted (Fig. 4c) forms of the regression coefficients are located off the western coast of South America.

Table 1 summarizes the values of L_i for several key area averages. The second column indicates the contribution of surface temperature variability over the indicated region to the global-mean internal feedback parameter, the third column indicates the contribution weighted by the fractional area of the globe, and the last column indicates the correlations, t scores, and significance based on a two-tailed test of the t statistic after accounting for the autocorrelations in the time series. The key results are the following:

- The negative contributions of the high-latitude continents to L_i are not statistically significant at the gridpoint scale (Fig. A1), but they are highly significant when averaged over all land areas (Table 1). The globally averaged land surface temperature accounts for roughly 70% of the global-mean negative internal feedback of −1.1 W m^{-2}.
- Globally averaged ocean temperatures (based on ERA5 2-m surface temperature over ocean areas) account for only about 30% of the global negative internal feedback, in part because the ocean areas are marked by competing regions of positive and negative feedbacks, and by small monthly surface temperature variances relative to land areas.
- Over equal-sized areas, the positive contributions to the global-mean internal feedback from the southeastern tropical Pacific and the negative contributions from the western tropical Pacific are comparable in amplitude.

The results in Fig. 4c and Table 1 highlight two key results that are not emphasized in Green's function experiments run on atmospheric models: 1) The land areas make a prominent contribution to the global internal feedback parameter and 2) the positive contributions to the global internal feedback over the eastern tropical Pacific have similar amplitude to the negative contributions over the western tropical Pacific. As discussed earlier, the feedbacks inferred from λ_i^R and thus L_i may reflect either (i) the relationships between R and local temperature and/or (ii) the relationships between R and temperatures at locations that covary with local temperature. Nevertheless, the inferred importance of land surface temperatures to the global-mean radiative response makes physical sense for at least two reasons: 1) Continental temperatures exhibit much larger variances on month-to-month time scales than ocean temperatures (e.g., Fig. 4b) and thus account for much of the covariability between R and T on intra-annual time scales; 2) Land surface temperatures account for ∼14% of the radiative response in a 4xCO_2 numerical simulation run with prescribed surface temperatures and thus have a seemingly important signature in the radiative response to climate change (Andrews et al. 2021). The differences between the contributions of land temperatures to the global feedback indicated in Table 1 and those indicated in Andrews et al. (2021) presumably derive in part from the associated patterns of surface temperature change: The results in Table 1 are based on internal variability in surface temperatures; the results in Andrews et al. (2021) are based on the surface temperature response to increasing CO_2. Notably, the role of the land surface cannot be inferred from the currently available Green's function experiments, since they are run using the AMIP protocol in which land surface temperatures are free running (Gates et al. 1999).

There are two possible reasons that atmospheric Green's function experiments indicate larger differences between the amplitudes of the feedbacks over the western and eastern tropical Pacific than those suggested in the observational results (Fig. 4c): 1) Atmospheric Green's function experiments are forced with similar amplitude SST anomalies at all locations (Bloch-Johnson et al. 2024), whereas the pattern in Fig. 4c is scaled relative to the internal variability, which is larger in the eastern tropical Pacific than in the western tropical Pacific (Fig. 4b), and 2) as shown in the next section, the positive covariability between R and the temperature field over the eastern tropical Pacific is underestimated in long control simulations run on many coupled-climate models.

5. Discussion

This section has four purposes:

1) To demonstrate that the method for computing L_i and its expansion coefficient time series is equivalent to maximum covariance analysis (MCA) and the first iteration of partial least squares (PLS) regression. The analogy indicates that L_i corresponds to the spatial pattern that explains the largest possible covariance between R and T_i.
2) To compare a) the contribution of the expansion coefficient time series of L_i to the global-mean radiative response with b) the contribution associated with the response function from a Green's function experiment.
3) To probe the ability of climate models to simulate L_i.

4) To compare the results with those derived from principal component analysis.

a. Relationship to maximum covariance analysis and partial least squares regression

The local feedback parameter λ_i^R—and its weighted analog L_i—indicates regions where surface temperature variability contributes to the global-mean radiative response and thus to the global-mean climate feedback. Since the pattern L_i is equivalent to the covariance between the temperature field T_i and the radiative response R [Eq. (6)], it follows that T_i can be projected onto L_i to form an estimate of the global-mean radiative response that is due entirely to variations in the surface temperature field. That is,

$$\hat{R}_L = T_i L_i, \tag{7}$$

where $\hat{R}_L$ denotes the estimate of the global-mean radiative flux found by projecting T_i onto L_i. Note that in the matrix operation above, T_i is the size $M \times N$, L_i is the size $N \times 1$, and $\hat{R}_L$ is the size $M \times 1$, where M is the number of time steps and N denotes the number of grid boxes.

The procedure for calculating L_i and its expansion coefficient time series $\hat{R}_L$ is equivalent to both MCA and the first iteration of partial least squares (PLS) regression. In MCA, the covariance matrix between two time-varying fields (M_i and N_i) is decomposed using singular value decomposition (SVD) to form a series of spatial maps in M_i (referred to as the singular vectors of M_i) that explain the variance in N_i, and vice versa (Bretherton et al. 1992). The singular vector of M_i that is associated with the largest singular value in the decomposition explains the maximum fraction of the covariance with N_i, and vice versa. In the case of L_i and $\hat{R}_L$, MCA is being conducted between the spatially varying surface temperature field T_i and the global-mean radiative response R. Since R is a function of time only, the covariance matrix $\overline{RT_i}$ corresponds to a vector, and the leading singular vector formed from MCA is simply $\overline{RT_i}$. Likewise, the covariance matrix $\overline{RT_i}$ and its expansion coefficient time series $\hat{R}_L$ are equivalent to the first iteration of PLS regression (e.g., Abdi 2010; Smoliak et al. 2015). Since L_i is proportional to the covariance between R and T_i [Eq. (6)], it follows that $\hat{R}_L$ has the same direction as the leading predictors formed from both MCA and PLS regression between R and T_i.

Why does this matter? The analogy to MCA and PLS regression indicates that L_i and $\hat{R}_L$ correspond to the pattern and expansion coefficient time series that explain the largest possible fraction of the covariance between T_i and R. Hence, L_i provides a basis for predicting R from variations in the temperature field. Figure 5a probes the ability of $\hat{R}_L$ to predict monthly mean variations in R in observations and 1200 years of preindustrial control output from the Max Planck Institute (MPI)-ESM1.2 (Table 2; Mauritsen et al. 2019; Rugenstein et al. 2019). All results are based on deseasonalized, monthly mean values of the data and output. The control output is not detrended since by construction there is no external forcing and thus $R = N$. The y axis denotes the correlations between the predicted and actual radiative responses ($\hat{R}_L$ and R); the x axis denotes the length of the period of record used to form L_i.

As a starting point, we consider the "in-sample" prediction derived from observations, where in-sample indicates that the pattern L_i is found from the same period used in the projection $\hat{R}_L = T_i L_i$. The predicted $\hat{R}_L$ time series is found for observations by projecting the observed T_i onto L_i from Fig. 4c. The correlation between the observed $\hat{R}_L$ and R is plotted in Fig. 5a at 25 years on the x axis (i.e., the length of the observational record). The 95% confidence bounds are found using a Fisher z transformation and accounting for the autocorrelation in the time series. The in-sample prediction of the observed R by the spatially varying temperature field is $r \approx 0.53$. That is, the time evolution of the pattern in Fig. 4c explains roughly 28% of the monthly mean variance in R over the CERES period of record.

We next consider the in-sample predictions derived from the output from the MPI-ESM1.2 preindustrial control simulation over a range of sample lengths. For reference, Fig. 5c shows the spatial pattern of L_i derived from all 1200 years of the MPI-ESM1.2 preindustrial control output. The pattern is characterized by negative values over much of the globe, with large negative values found over land areas and a notable lack of positive values over the eastern tropical Pacific. The in-sample predictions provided by $\hat{R}_L$ are shown in the blue dots and are found as follows. For a given sample length n, we 1) calculate L_i in all nonoverlapping samples of length n. Note that the L_i can vary from one sample to the next; 2) form $\hat{R}_L$ in all samples by projecting the in-sample T_i onto the in-sample L_i; and 3) calculate the correlations between R and $\hat{R}_L$ in each sample and then average the correlations over all samples (the average correlations are found as $\sqrt{\overline{r^2}}$, where r denotes the sample correlations, and the overline denotes the sample mean). The error bars indicate the 95% confidence bounds found using the Fisher z transformation. Note the error bars are smaller than those for the observations since the correlations are averaged over multiple independent samples. The in-sample prediction of R by MCA is roughly $r = 0.51$ when L_i and $\hat{R}_L$ are formed from samples that are 20 years long (240 months) and decreases to roughly $r = 0.39$ for samples that are 100 years long. Hence, $\hat{R}_L$ explains roughly 25% of the variance in monthly mean R for sample sizes of 20 years and about 15% of the variance for sample sizes longer than 100 years. The correlations between R and $\hat{R}_L$ decrease as the sample size increases. Note that the correlation between R and $\hat{R}_L$ derived from observations is larger than the correlation derived from MPI-ESM1.2 control output at a sample length of 25 years, but that the model output nevertheless lies within the error bars of the observed correlation.

The results in the blue dots are based on in-sample correlations and are thus susceptible to overfitting. That is, L_i explains the largest fraction of the covariance between R and T_i, but some of the structure in L_i is inevitably due to sampling variability and thus not stationary from one period to the next. Hence, in the red dots, we show the out-of-sample correlations between R and $\hat{R}_L$, where the projection $\hat{R}_L = T_i L_i$ is done over a different period than that used to form the pattern L_i. In this case, for a given sample length n, we 1) define a training period of length n during the first 600 years of the simulation, 2) calculate L_i during the training period, 3) form $\hat{R}_L$ by projecting temperature during the last 600 years of the

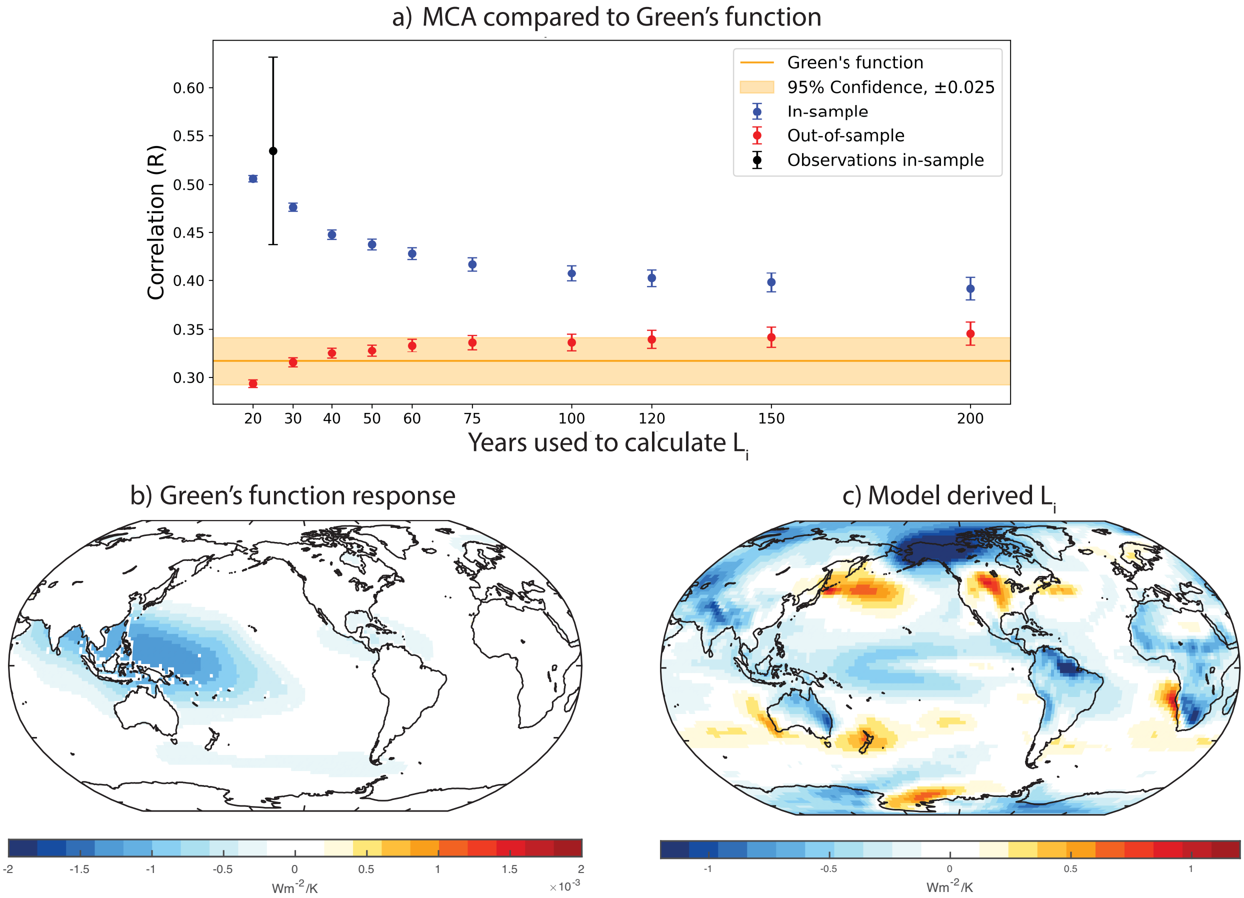

FIG. 5. (a) Dots: correlations between (a) the global-mean radiative flux and (b) the global-mean radiative flux predicted by projecting T_i onto L_i [Eq. (7)]. The black dot indicates in-sample results for the observations, where in-sample indicates that the projection of T_i onto L_i is performed during the same period used to calculate L_i. The blue and red dots indicate in-sample and out-of-sample results, respectively, based on 1200 years of PI control output from the MPI-ESM1.2. The x axis denotes the length of the sample size used in the analysis. Horizontal line: correlation between (a) the global-mean radiative flux and (b) the global-mean radiative flux predicted by projecting T_i onto the Green's function G_i from Alessi and Rugenstein (2023) over the last 600 years of the control integration. Error bars denote the 95% confidence ranges based on one sample for the observations, the number of nonoverlapping samples available from the control output (red and blue dots), and the range of uncertainty in the Green's function prediction. See text for details. (b) Global-mean radiative response to perturbations in regional temperature derived from the Green's function experiments in Alessi and Rugenstein (2023). The pattern in (b) is used to generate the horizontal line in (a). (c) The pattern of L_i calculated from 1200 years of control output from the MPI-ESM1.2. Versions of the pattern in (c) based on subsamples of the control output are used to generate the dots in the top panel.

simulation (the test period) onto L_i, 4) calculate the correlations between R and $\hat{R}_L$ during the test period, and 5) repeat the analysis over all possible nonoverlapping training periods of length n during the first 600 years. The out-of-sample predictions of R by MCA are—as expected—notably less than they are for the in-of-sample case. The correlations between R and $\hat{R}_L$ are roughly $r = 0.29$ for a sample size of 20 years and asymptote to $r \approx 0.34$ for a 100-yr period of record. In contrast to the in-sample case, the correlations for the out-of-sample case increase with sample size since the amount of data used to generate L_i (i.e., the size of the training sample) increases.

The key take-home messages from the above are that 1) L_i and its expansion coefficient time series $\hat{R}_L = T_i L_i$ correspond to the leading patterns formed from both MCA and PLS regression between the temperature field and global-mean radiation. Hence, the spatial feedback pattern L_i introduced here corresponds to the spatial structure in T_i that explains a largest possible fraction of covariance between R and T_i, and 2) for the out-of-sample case, the spatial feedback pattern L_i explains roughly $r^2 \approx 0.34^2 \approx 12\%$ of the variance in R when the sample size exceeds ~100 years. The out-of-sample correlations appear at first glance small: They indicate that roughly 90% of the variance in monthly mean R is not explained by the time evolution of the leading temperature pattern derived from MCA (and PLS regression) between R and T_i. However, as shown below, the variance explained by MCA nevertheless exceeds that provided by output from a Green's function experiment.

TABLE 2. Preindustrial control simulations from LongRunMIP used in Figs. 5 and 6 (full references are provided in Table 2 of Rugenstein et al. 2019).

Model identification	PiControl length (yr)
CCSM3	3805
CESM1.0.4	1000
CNRM-CM6-1	2000
GFDL CM3	5200
GFDL-ESM2M	1340
IPSL-CM5A-LR	1000
MIROC3.2	681
MPI-ESM1.2	1237

b. *Comparison with output from an atmospheric Green's function experiment*

The Green's function approach provides a Jacobian of the simulated radiative response to temperature variations at all locations $\partial R_i/\partial T_i$. When globally averaged, it provides a spatial pattern $G_i \equiv (\partial R/\partial T_i)$ that indicates the simulated response of the global-mean radiative flux to variations in temperature at a given location. The distinctions between the "response function" provided by the Green's function approach (G_i) and that provided by MCA (L_i) can be conceptualized as follows: At a given location, results based on L_i arise not only from the relationships between R and local temperatures but also—due to the spatial structure of covariability in the temperature field—from the relationships between R and temperatures at all other locations where the temperature field covaries with local temperature. In contrast, results based on G_i isolate the relationships between R and local temperatures. Put another way, the pattern L_i may be viewed as a "statistical" response function of R to T_i, where T_i includes spatially varying covariability embedded in the temperature field; the pattern G_i may be viewed as a "causal" response function of R to T_i, where T_i is prescribed and thus only exhibits spatial structure if such covariability is prescribed in the experiment procedure.

Here, we compare the results derived from MCA (and thus PLS regression) to those derived from the Green's function experiments described in Alessi and Rugenstein (2023). The experiments in Alessi and Rugenstein (2023) are run on the same atmospheric model used in the coupled ocean/atmosphere control experiment analyzed in the previous section (MPI ECHAM6) and thus allow us to test results based on L_i with those derived from G_i using the same atmospheric model. The spatial pattern of G_i from the experiments in Alessi and Rugenstein (2023) is shown in their Fig. 1a and reproduced here in Fig. 5b. As is the case for other Green's function-type experiments (e.g., Dong et al. 2019), the Green's function response is dominated by negative relationships between T_i and R over the western tropical Pacific. The G_i (Fig. 5b) and L_i (Fig. 5c) patterns derived from the MPI numerical model both exhibit negative values in the tropical Pacific, but exhibit notable differences elsewhere, in particular the L_i pattern exhibits large negative values over land areas.

The global-mean radiative response predicted by the time evolution of the Green's function pattern in Fig. 5b can be found in a similar manner to Eq. (7):

$$\hat{R}_G = T_i G_i, \tag{8}$$

where $\hat{R}_G$ denotes the estimate of the global-mean radiative flux derived by projecting T_i from the control simulation onto G_i. The horizontal line in Fig. 5a shows the correlation between $\hat{R}_G$ and R over the 600-yr period of record from the MPI-ESM1.2 control simulations (i.e., the same period used to test the out-of-sample MCA). The Green's function approach yields a correlation between the actual and predicted global-mean radiative flux of $r \sim 0.3$. Consistent with the discussion of MCA above, the in-sample correlations provided by L_i exceed those provided by G_i regardless of the sample size. For the out-of-sample case, the error bars on the predictive skill afforded by the Green's function approach overlap those associated with MCA for sample sizes greater than roughly 30 years. The key result in Fig. 5 is thus that—for sample sizes greater than a few decades—MCA yields effectively the same predictive skill for monthly mean variations in TOA radiation as that provided by the Green's function found from fixed SST experiments run on the same atmospheric model. Note that results in Fig. 5 are based on a statistical response function L_i estimated from—and applied to—the radiative response to internal variability. In a companion study (L. Fredericks et al. 2025, unpublished manuscript), we explore the ability of MCA and other statistical methods to estimate the radiative response to greenhouse gas forcing.

The correlations between the actual radiative flux R and that predicted by the Green's function approach $\hat{R}_G$ indicated in Fig. 5 are weaker than those reported in Dong et al. (2019) and Alessi and Rugenstein (2023). Dong et al. (2019) report correlations in excess of $r \approx 0.9$ between their R and $\hat{R}_G$; Alessi and Rugenstein (2023) report correlations approaching $r \approx 0.5$. Several factors contribute to these differences. First, the results in Dong et al. (2019) are based on comparisons with R formed from prescribed SST experiments rather than a coupled atmosphere/ocean GCM. Their results confirm the linearity of the radiative response to SST patches but do not prove the ability of the Green's function approach to reproduce observed, internal variability in R. Second, the results in Dong et al. (2019) and Alessi and Rugenstein (2023) are based on annual-mean output, whereas the results here are based on monthly mean output which includes considerably more variance in R.

c. *Spatial patterns of the local feedback λ_i^R in preindustrial control simulations*

A central feature arising from the observational analyses in the previous sections is the large positive correlations between local temperature and the global-mean radiative flux over the eastern tropical Pacific. Figure 6 probes the ability of climate models to reproduce the observed relationships between R and temperatures in this region. The upper panels in Fig. 6 show λ_i^R calculated from eight preindustrial control simulations run under the auspices of Long Run Model Intercomparison Project (LongRunMIP) (see Table 2 here and Rugenstein et al. 2019; note that the λ_i^R map for the MPI-ESM1.2 is derived from the same output used to generate the L_i map in Fig. 5c). As indicated in the regression maps and summarized in the violin plots

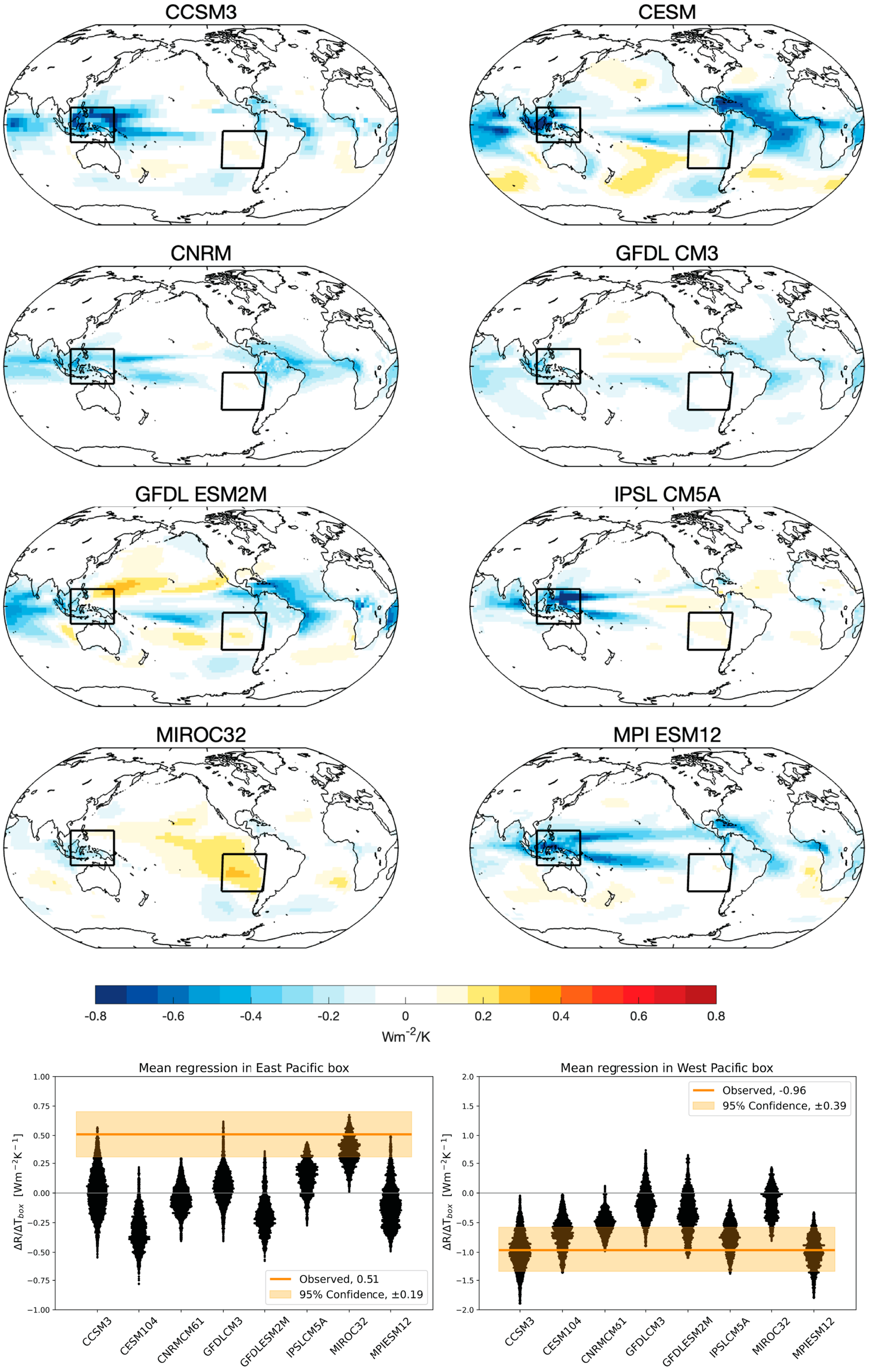

FIG. 6. (first row– fourth row) The local parameter λ_i^R as in Figs. 2a and Fig. 4a, but for climate models archived via LongRunMIP that have long (>600-yr) preindustrial control simulations (Table 1). Boxes indicate the equivalent-sized areas used to generate the results in the bottom row: 110°–150°E and 14°N–14°S in the western tropical Pacific and 110°–70°W and 5°–35°S in the eastern tropical Pacific. (bottom row) Red line: regression coefficients averaged over the western and eastern tropical Pacific (boxed areas in upper panels) based on observations. Black violin plots: regression coefficients averaged over the boxed areas calculated from all possible consecutive 298-month periods in the control model output (the length of the observational record is also 298 months). The 95% confidence interval for the observed values is found from the standard error of the regression.

at the bottom of Fig. 6, the climate models listed in Table 2 generally reproduce the region of negative covariability between T_i and R over the western tropical Pacific in 25-yr subsamples of the output (i.e., subsamples comparable to the length of the observational record). However, they generally do not reproduce the robust positive covariability between T_i and R over the eastern tropical Pacific. Of the eight models considered in Fig. 6, positive regression coefficients that overlap the observational uncertainty arise in less than roughly 1% of all 25-yr samples in four models and in less than roughly 5% of all 25-yr samples in another three models. Only the MIROC control simulation yields values of λ_i^R over the eastern tropical Pacific that match observations in a majority of all samples.

Most Green's function experiments indicate positive contributions from surface temperatures over the eastern tropical Pacific to the global-mean radiative feedback (Bloch-Johnson et al. 2024, cf. Fig. 2). However, the results shown in Fig. 6 clearly indicate that the LongRunMIP simulations do not reproduce the observed covariability between surface temperatures over the eastern tropical Pacific region and the global-mean radiative flux on monthly mean time scales. The differences between the observed (Fig. 2a) and modeled (Fig. 6) relationships between R and temperatures over the eastern tropical Pacific may reflect biases in the model radiative response to SST anomalies in the eastern Pacific, or they may reflect biases in model representations of the patterns of internal climate variability; i.e., λ_i^R is influenced by the spatial patterns of variability in the monthly varying temperature field. It would be interesting to compare the observed λ_i^R with that derived from AMIP-style prescribed SST experiments, in which the spatial coherence of the SST field is by construction identical in the simulation and observations.

d. *Comparison with results based on principal component analysis*

As discussed above, the analysis applied here (i.e., MCA or PLS regression between T_i and R) is not directly comparable to results derived from Green's function experiments. That is because MCA and PLS regression retain the spatial coherence of the temperature field, whereas Green's function experiments hold temperature fixed at all locations other than the forcing region. However, an analogy can be drawn between the Green's function approach and multilinear regression (MLR), whereby the global radiative response is treated as the linear combination of independent responses to temperature at all separate locations. Since MCA and PLS regression are solutions to the MLR problem, it follows that they are conceptually related to the Green's function approach. We have also reproduced the analysis here using the ordinary least squares (OLS) solution to MLR, and the results are explored in a companion study (L. Fredericks et al. 2025, unpublished manuscript). In short, for sample sizes comparable to the observed record, the OLS solution to MLR reproduces the broad features found in MCA, including the regions of positive coefficients over the eastern Pacific and negative coefficients over the western Pacific. The OLS solution provides better predictive skill than MCA, but the results are also more sensitive to overfitting.

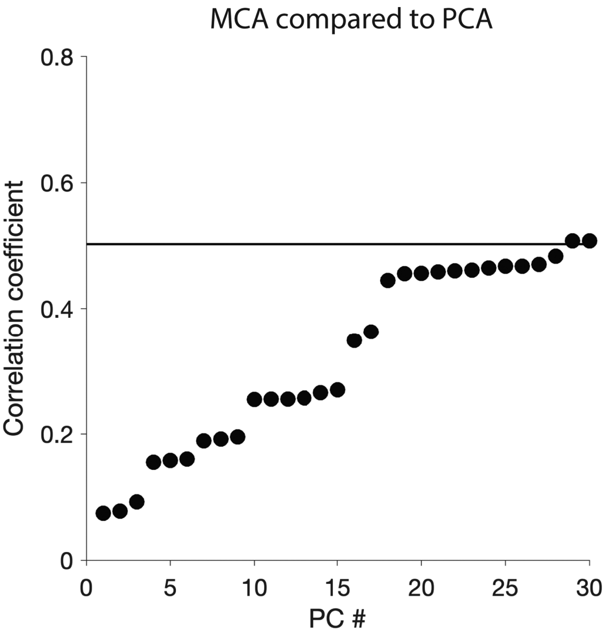

FIG. 7. Comparing the prediction of R provided by MCA and PCA. The horizontal line shows the correlation between R and the expansion coefficient time series of L_i from Fig. 4c. The dots show the cumulative correlations between the PCs of the ERA5 2-m temperature field and R, where the cumulative correlations are found as the square root of the sum of the squared correlations. Roughly, the first 26 PCs of the temperature field are required to match the explanatory power of MCA.

The robustness of the MCA (and PLS regression) solution highlighted here is exemplified by comparing the results with those derived from the leading principal components (PCs) of the temperature field. The advantage of using PCs is that they retain the spatial structure inherent in the temperature field, and they also provide an orthogonal basis set of predictors. The results based on PC analyses of T_i from ERA5 are shown in Fig. 7 and are formed as follows. The horizontal line shows the correlation between R and the expansion coefficient time series derived from MCA analysis, that is, the correlation between R and $R_L = T_i L_i$, where L_i is shown in Fig. 4c. The dots show the cumulative correlations between R and the PCs of the ERA5 near-surface temperature field, where the cumulative correlations are found as $\sqrt{\sum_i r^2(\mathrm{PC}_i, R)}$. For example, the correlation between R and PC_1 is $r = 0.16$, and the cumulative correlation between R and PCs 1–10 is $r = 0.43$. As evidenced in the figure, roughly the first 26 PCs of the temperature field are required to match the explanatory power of MCA. A similar comparison between MCA and PC analyses was conducted in Thompson et al. (2009) for the case of the spatially varying pressure field and hemispheric mean surface temperature (see their Fig. 3).

6. Conclusions

Spatially varying radiative feedbacks are commonly assessed using two different regression-based parameters

(Feldl and Roe 2013; Sherwood et al. 2020; Hedemann et al. 2022): the local radiative response regressed on local temperature $\lambda_i^L = (\Delta R_i/\Delta T_i)$ and the local radiative response regressed on global-mean temperature $\lambda_i^T = (\Delta R_i/\Delta T)$. Both have been widely explored in previous work. Here, we have explored the insights provided by an alternative spatially varying parameter: the global-mean radiative response regressed on local temperature: $\lambda_i^R = (\Delta R/\Delta T_i)$. When estimated from linear least squares regression between R and T_i, the parameter is found as $\lambda_i^R = (\overline{RT_i}/\overline{T_i^2})$.

The λ_i^R parameter highlights regions where surface temperature covaries with the global-mean radiative response. The parameter yields physically meaningful structures when estimated from monthly mean observations of CERES radiative fluxes and surface temperatures. It confirms that anomalously warm surface conditions in regions of tropical deep convection are associated with anomalously upward global-mean radiative fluxes, consistent with negative climate feedbacks associated with temperature variability in these regions. Notably, it also indicates that warm conditions over the southeastern tropical Pacific are associated with similarly large downward global-mean radiative fluxes, consistent with positive climate feedbacks due to temperature variability there.

The λ_i^R parameter can be transformed into a form that can be globally averaged by multiplying it by the ratio of the local to global-mean temperature variance. The weighted parameter $L_i \equiv \lambda_i^R(\overline{T_i^2}/\overline{T^2}) = (\overline{RT_i}/\overline{T^2})$ provides estimates of the contribution of the local temperature field to the global feedback. The pattern L_i may be viewed as a statistical response function that is analogous to the causal response functions provided by atmospheric Green's function experiments forced with prescribed changes in SSTs. The differences between the two response functions lie in the interpretation: The statistical response function L_i reflects the linkages between local surface temperature variability and the global-mean radiative response and is independent of whether the feedbacks are occurring locally, or over regions where the temperature field covaries with local temperature. The causal response function given by the Green's function approach derives entirely from the global-mean radiative response to the prescribed SSTs (or the associated changes in the free-running land surface temperature). The advantage of the statistical response function highlighted here is that it accounts for the naturally occurring patterns of internal variability in the temperature field. The disadvantage is that it does not uniquely isolate the specific regions associated with the underlying feedbacks.

The results of the statistically based response function L_i indicate that 1) the contribution of temperature variability in the southeastern tropical Pacific to positive values in the global internal feedback parameter is comparable to 2) the contribution of temperature variability in the western tropical Pacific to negative values in the global feedback parameter. They also indicate that variability in global-mean land temperatures contributes to roughly 70% of the global-mean, negative internal feedback. In contrast, Green's function experiments indicate that the positive feedbacks over the eastern tropical Pacific are generally weaker than the negative feedbacks found over the western Pacific. The existing Green's function experiments also do not consider the role of surface temperature feedbacks over land areas since they are forced only by temperature patches over the oceans.

The parameter L_i is equivalent to the leading pattern formed from MCA and PLS regression between surface temperature field and the global-mean radiative response R. Hence, the expansion coefficient time series formed by projecting temperatures onto L_i, that is, $\hat{R}_L = T_i L_i$, explains a larger fraction of the covariance between R and T_i than that associated with any other pattern in the temperature field. For example, roughly the first ~25 PCs of the surface temperature field are required to match the variance in the global-mean radiative flux that is explained by the single temperature pattern derived from MCA and PLS regression. We tested the ability of $\hat{R}_L$ to explain variations in the global-mean radiative flux in 1200 years of output from a coupled atmosphere/ocean model simulation and compared its performance to the output from an atmospheric Green's function experiment run on the same version of the atmospheric component of the coupled model. For sample sizes longer than ~30 years, the out-of-sample prediction of monthly mean values of R by the pattern L_i is statistically indistinguishable from that provided by output from the Green's function experiment. We also probed the ability of climate models to reproduce λ_i^R and L_i. The relationships between R and temperatures over the southeastern tropical Pacific are notably underestimated in all but one of the eight control simulations considered here.

As is the case for any observational study of global climate feedbacks, the results here are limited to the CERES era, in our case 25 years. They are thus more susceptible to sampling variability than results based on, say, long simulations run on climate models. Nevertheless, the robustness of the key features revealed by λ_i^R—particularly the positive values over the eastern tropical Pacific, negative values over the western tropical Pacific, and negative values over the land areas—is supported by several sensitivity tests. The key tropical features are associated with t scores that exceed $|3|$, are reproducible in seasonally stratified subsets of the data, are reproducible in annual-mean versions of the data, and are not sensitive to the choice of removing F by either (i) detrending N or (ii) subtracting the AR6 radiative forcing estimate from N. The negative feedbacks over the land areas are not significant at the gridbox level due to the large amount of internal variability at the local scale, but they are highly significant when averaged over large spatial areas. Regression dilution is expected to bias the amplitudes of the linear regression coefficients, but it does not affect the sign of the regression and thus the general spatial structure of λ_i^R. It does not affect the pattern of L_i since the covariance is commutative.

Overall, the results shown here provide a statistical framework for assessing the temperature pattern effect on the global-mean radiative response in observations and models; reveal the prominence of positive internal feedbacks due to temperature variability in the eastern tropical Pacific; and highlight the importance of the land areas in governing the amplitude of the global-mean, negative internal feedback.

Acknowledgments. We thank the Editor Robert Christopher Jnglin Wills, three anonymous reviewers, and an anonymous associate editor for their constructive, detailed, and helpful comments on the manuscript. We also thank Jonathan Gregory and Paulo Ceppi for helpful discussion of the results. D. W. J. T. is supported by the National Aeronautics and Space Administration (NASA) under 80NSSC23K0113 and the NSF CLD Program under AGS-2116186. M. R. is funded by NASA under 80NSSC21K1042 and by NSF CLD under AGS-2233673. L. F. is supported by the NSF Climate and Large-Scale Dynamics program under AGS-2116186 and AGS-2233673, and NASA FINESST Award 80NSSC24K0024.

Data availability statement. All data used in the study are publicly available as noted in the manuscript. The ERA5 reanalysis data are available at https://cds.climate.copernicus.eu/. The CERES data are available at https://ceres.larc.nasa.gov/data/. The numerical output is listed in Table 2 and available through the LongRunMIP project. Programming scripts are available at https://doi.org/10.5281/zenodo.15190027 and https://doi.org/10.5281/zenodo.15192484.

APPENDIX

Significance of Figure 2a

The top panel in Fig. A1 is based on the same data used in Fig. 2a but shows the correlations rather than regressions between global-mean net TOA radiative fluxes R and local surface temperature anomalies T_i. Results are based on monthly mean, detrended values of CERES radiative fluxes and ERA5 2-m temperature. The bottom panel shows the corresponding t scores, where the effective sample size is found after accounting for the autocorrelations in both the R and T_i time series. The t scores are shown for values greater than 2. The t scores $> |2|$ are significant at the 95% level based on a two-tailed test of the t statistic; t scores $> |2.6|$ are significant at the 99% level. Results over the southeastern tropical Pacific include t scores $> |4|$.

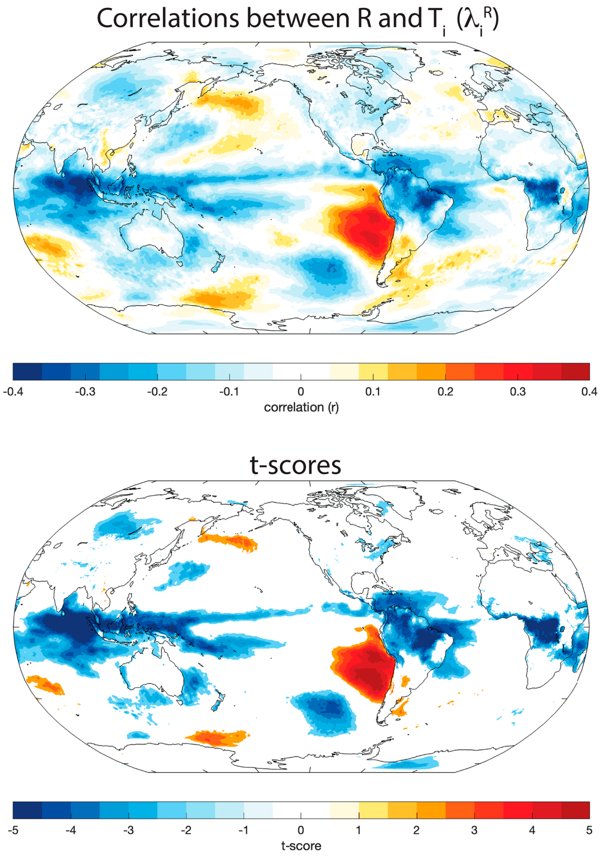

Correlations between R and T_i (λ_i^R)

t-scores

FIG. A1. (top) Correlations between global-mean net TOA radiative fluxes R and local surface temperature anomalies T_i. (bottom) The t scores for the correlation coefficients shown in the (top). As in Fig. 2, results are based on monthly mean, detrended values of CERES radiative fluxes and ERA5 2-m temperature. The t scores are shown for values greater than 2. The t scores > 2 are significant at the 95% level based on a two-tailed test of the t statistic; t scores > 2.6 are significant at the 99% level.

REFERENCES

Abdi, H., 2010: Partial least squares regression and projection on latent structure regression (PLS Regression). *WIREs Comput. Stat.*, **2**, 97–106, https://doi.org/10.1002/wics.51.

Alessi, M. J., and M. A. A. Rugenstein, 2023: Surface temperature pattern scenarios suggest higher warming rates than current projections. *Geophys. Res. Lett.*, **50**, e2023GL105795, https://doi.org/10.1029/2023GL105795.

Andrews, T., and M. J. Webb, 2018: The dependence of global cloud and lapse rate feedbacks on the spatial structure of tropical Pacific warming. *J. Climate*, **31**, 641–654, https://doi.org/10.1175/JCLI-D-17-0087.1.

——, J. M. Gregory, and M. J. Webb, 2015: The dependence of radiative forcing and feedback on evolving patterns of surface temperature change in climate models. *J. Climate*, **28**, 1630–1648, https://doi.org/10.1175/JCLI-D-14-00545.1.

——, C. J. Smith, G. Myhre, P. M. Forster, R. Chadwick, and D. Ackerley, 2021: Effective radiative forcing in a GCM with fixed surface temperatures. *J. Geophys. Res. Atmos.*, **126**, e2020JD033880, https://doi.org/10.1029/2020JD033880.

——, and Coauthors, 2022: On the effect of historical SST patterns on radiative feedback. *J. Geophys. Res. Atmos.*, **127**, e2022JD036675, https://doi.org/10.1029/2022JD036675.

Armour, K. C., C. M. Bitz, and G. H. Roe, 2013: Time-varying climate sensitivity from regional feedbacks. *J. Climate*, **26**, 4518–4534, https://doi.org/10.1175/JCLI-D-12-00544.1.

Barsugli, J. J., and P. D. Sardeshmukh, 2002: Global atmospheric sensitivity to tropical SST anomalies throughout the Indo-Pacific basin. *J. Climate*, **15**, 3427–3442, https://doi.org/10.1175/1520-0442(2002)015<3427:GASTTS>2.0.CO;2.

Bloch-Johnson, J., M. Rugenstein, and D. S. Abbot, 2020: Spatial radiative feedbacks from internal variability using multiple regression. *J. Climate*, **33**, 4121–4140, https://doi.org/10.1175/JCLI-D-19-0396.1.

——, and Coauthors, 2024: The Green's Function Model Intercomparison Project (GFMIP) protocol. *J. Adv. Model. Earth Syst.*, **16**, e2023MS003700, https://doi.org/10.1029/2023MS003700.

Boer, G., and B. Yu, 2003: Climate sensitivity and response. *Climate Dyn.*, **20**, 415–429, https://doi.org/10.1007/s00382-002-0283-3.

Branstator, G., 1985: Analysis of general circulation model sea-surface temperature anomaly simulations using a linear model. Part I: Forced solutions. *J. Atmos. Sci.*, **42**, 2225–2241, https://doi.org/10.1175/1520-0469(1985)042<2225:AOGCMS>2.0.CO;2.

Bretherton, C. S., C. Smith, and J. M. Wallace, 1992: An intercomparison of methods for finding coupled patterns in climate data. *J. Climate*, **5**, 541–560, https://doi.org/10.1175/1520-0442(1992)005<0541:AIOMFF>2.0.CO;2.

Ceppi, P., and J. M. Gregory, 2017: Relationship of tropospheric stability to climate sensitivity and Earth's observed radiation budget. *Proc. Natl. Acad. Sci. USA*, **114**, 13 126–13 131, https://doi.org/10.1073/pnas.1714308114.

——, and S. Fueglistaler, 2021: The El Niño–Southern Oscillation pattern effect. *Geophys. Res. Lett.*, **48**, e2021GL095261, https://doi.org/10.1029/2021GL095261.

Dessler, A. E., and P. M. Forster, 2018: An estimate of equilibrium climate sensitivity from interannual variability. *J. Geophys. Res. Atmos.*, **123**, 8634–8645, https://doi.org/10.1029/2018JD028481.

Dong, Y., C. Proistosescu, K. C. Armour, and D. S. Battisti, 2019: Attributing historical and future evolution of radiative feedbacks to regional warming patterns using a Green's function approach: The preeminence of the western Pacific. *J. Climate*, **32**, 5471–5491, https://doi.org/10.1175/JCLI-D-18-0843.1.

——, and Coauthors, 2021: Biased estimates of equilibrium climate sensitivity and transient climate response derived from historical CMIP6 simulations. *Geophys. Res. Lett.*, **48**, e2021GL095778, https://doi.org/10.1029/2021GL095778.

Feldl, N., and G. H. Roe, 2013: Four perspectives on climate feedbacks. *Geophys. Res. Lett.*, **40**, 4007–4011, https://doi.org/10.1002/grl.50711.

Forster, P., and Coauthors, 2021: The Earth's energy budget, climate feedbacks and climate sensitivity. *Climate Change 2021: The Physical Science Basis*, V. Masson-Delmotte et al., Eds., Cambridge University Press, 923–1054, https://doi.org/10.1017/9781009157896.009.

Frost, C., and S. G. Thompson, 2000: Correcting for regression dilution bias: Comparison of methods for a single predictor variable. *J. Roy. Stat. Soc.*, **163A**, 173–189, https://doi.org/10.1111/1467-985X.00164.

Gates, W. L., and Coauthors, 1999: An overview of the results of the Atmospheric Model Intercomparison Project (AMIP I). *Bull. Amer. Meteor. Soc.*, **80**, 29–55, https://doi.org/10.1175/1520-0477(1999)080<0029:AOOTRO>2.0.CO;2.

Gregory, J. M., and T. Andrews, 2016: Variation in climate sensitivity and feedback parameters during the historical period. *Geophys. Res. Lett.*, **43**, 3911–3920, https://doi.org/10.1002/2016GL068406.

Gregory, J. M., T. Rews, P. Ceppi, T. Mauritsen, and M. J. Webb, 2020: How accurately can the climate sensitivity to CO_2 be estimated from historical climate change?. *Climate Dyn.*, **54**, 129–157, https://doi.org/10.1007/s00382-019-04991-y.

Gregory, J. M., and Coauthors, 2004: A new method for diagnosing radiative forcing and climate sensitivity. *Geophys. Res. Lett.*, **31**, L03205, https://doi.org/10.1029/2003GL018747.

Hansen, J., M. Sato, and R. Ruedy, 1997: Radiative forcing and climate response. *J. Geophys. Res.*, **102**, 6831–6864, https://doi.org/10.1029/96JD03436.

Hedemann, C., T. Mauritsen, J. Jungclaus, and J. Marotzke, 2022: Reconciling conflicting accounts of local radiative feedbacks in climate models. *J. Climate*, **35**, 3131–3146, https://doi.org/10.1175/JCLI-D-21-0513.1.

Hersbach, H., and Coauthors, 2020: The ERA5 global reanalysis. *Quart. J. Roy. Meteor. Soc.*, **146**, 1999–2049, https://doi.org/10.1002/qj.3803.

Klein, S. A., and D. L. Hartmann, 1993: The seasonal cycle of low stratiform clouds. *J. Climate*, **6**, 1587–1606, https://doi.org/10.1175/1520-0442(1993)006<1587:TSCOLS>2.0.CO;2.

Loeb, N. G., and Coauthors, 2018: Clouds and the Earth's Radiant Energy System (CERES) Energy Balanced and Filled (EBAF) Top-of-Atmosphere (TOA) edition-4.0 data product. *J. Climate*, **31**, 895–918, https://doi.org/10.1175/JCLI-D-17-0208.1.

——, and Coauthors, 2022: Evaluating twenty-year trends in Earth's energy flows from observations and reanalyses. *J. Geophys. Res. Atmos.*, **127**, e2022JD036686, https://doi.org/10.1029/2022JD036686.

Lutsko, N. J., and K. Takahashi, 2018: What can the internal variability of CMIP5 models tell us about their climate sensitivity? *J. Climate*, **31**, 5051–5069, https://doi.org/10.1175/JCLI-D-17-0736.1.

Mauritsen, T., and Coauthors, 2019: Developments in the MPI-M Earth System Model version 1.2 (MPI-ESM1.2) and its response to increasing CO_2. *J. Adv. Model. Earth Syst.*, **11**, 998–1038, https://doi.org/10.1029/2018MS001400.

Morice, C. P., and Coauthors, 2021: An updated assessment of near-surface temperature change from 1850: The HadCRUT5 data set. *J. Geophys. Res. Atmos.*, **126**, e2019JD032361, https://doi.org/10.1029/2019JD032361.

Myers, T. A., R. C. Scott, M. D. Zelinka, S. A. Klein, J. R. Norris, and P. M. Caldwell, 2021: Observational constraints on low cloud feedback reduce uncertainty of climate sensitivity. *Nat. Climate Change*, **11**, 501–507, https://doi.org/10.1038/s41558-021-01039-0.

——, M. D. Zelinka, and S. A. Klein, 2023: Observational constraints on the cloud feedback pattern effect. *J. Climate*, **36**, 6533–6545, https://doi.org/10.1175/JCLI-D-22-0862.1.

Park, S., and C. B. Leovy, 2004: Marine low-cloud anomalies associated with ENSO. *J. Climate*, **17**, 3448–3469, https://doi.org/10.1175/1520-0442(2004)017<3448:MLAAWE>2.0.CO;2.

Proistosescu, C., A. Donohoe, K. C. Armour, G. H. Roe, M. F. Stuecker, and C. M. Bitz, 2018: Radiative feedbacks from stochastic variability in surface temperature and radiative imbalance. *Geophys. Res. Lett.*, **45**, 5082–5094, https://doi.org/10.1029/2018GL077678.

Rugenstein, M., and Coauthors, 2019: LongRunMIP: Motivation and design for a large collection of millennial-length AOGCM simulations. *Bull. Amer. Meteor. Soc.*, **100**, 2551–2570, https://doi.org/10.1175/BAMS-D-19-0068.1.

Rugenstein, M. A. A., and K. C. Armour, 2021: Three flavors of radiative feedbacks and their implications for estimating equilibrium climate sensitivity. *Geophys. Res. Lett.*, **48**, e2021GL092983, https://doi.org/10.1029/2021GL092983.

Sherwood, S. C., and Coauthors, 2020: An assessment of Earth's climate sensitivity using multiple lines of evidence. *Rev. Geophys.*, **58**, e2019RG000678, https://doi.org/10.1029/2019RG000678.

Smoliak, B. V., J. M. Wallace, P. Lin, and Q. Fu, 2015: Dynamical adjustment of the Northern Hemisphere surface air temperature field: Methodology and application to observations. *J. Climate*, **28**, 1613–1629, https://doi.org/10.1175/JCLI-D-14-00111.1.

Stevens, B., S. C. Sherwood, S. Bony, and M. J. Webb, 2016: Prospects for narrowing bounds on Earth's equilibrium climate sensitivity. *Earth's Future*, **4**, 512–522, https://doi.org/10.1002/2016EF000376.

Thompson, D. W. J., J. M. Wallace, P. D. Jones, and J. J. Kennedy, 2009: Identifying signatures of natural climate variability in time series of global-mean surface temperature: Methodology and insights. *J. Climate*, **22**, 6120–6141, https://doi.org/10.1175/2009JCLI3089.1.

Wood, R., and C. S. Bretherton, 2006: On the relationship between stratiform low cloud cover and lower-tropospheric stability. *J. Climate*, **19**, 6425–6432, https://doi.org/10.1175/JCLI3988.1.

Zhang, B., M. Zhao, and Z. Tan, 2023: Using a Green's function approach to diagnose the pattern effect in GFDL AM4 and CM4. *J. Climate*, **36**, 1105–1124, https://doi.org/10.1175/JCLI-D-22-0024.1.

Zhou, C., M. D. Zelinka, and S. A. Klein, 2016: Impact of decadal cloud variations on the Earth's energy budget. *Nat. Geosci.*, **9**, 871–874, https://doi.org/10.1038/ngeo2828.

——, ——, and ——, 2017: Analyzing the dependence of global cloud feedback on the spatial pattern of sea surface temperature change with a Green's function approach. *J. Adv. Model. Earth Syst.*, **9**, 2174–2189, https://doi.org/10.1002/2017MS001096.

——, ——, A. E. Dessler, and M. Wang, 2021: Greater committed warming after accounting for the pattern effect. *Nat. Climate Change*, **11**, 132–136, https://doi.org/10.1038/s41558-020-00955-x.